

Article

Numerical and Experimental Study of Low-Frequency Membrane Damper for Tube Vibration Suppression

Boris I¹  and Jaesun Lee^{2,*} ¹ Department of Smart Manufacturing, Changwon National University, Changwon 51140, Republic of Korea; ee.boris@changwon.ac.kr² School of Mechanical Engineering, Changwon National University, Changwon 51140, Republic of Korea

* Correspondence: jaesun@changwon.ac.kr

Abstract: In modern days, low-frequency vibration is still challenging to suppress due to its high vibrational energy. A typical suppression method is to increase the object's mass to reduce the amplitude of the vibration, but such a way is unsuitable in many cases. Membrane dampers can potentially eliminate the limitation and offer lightweight and compact damper. The idea is to decrease the stiffness and add additional mass made of silicone rubber were used for the damper. Finite element eigenfrequency simulation showed the transformation of each mode to the damper mode, where the tube displacement was zero. Also, it showed the bandgap between modes in the frequency range from 106 Hz to 158 Hz. The experimental verification of clamped from both ends of the tube showed the predicted bandgap and absence of the resonance peak of the bare tube. Overall, the membrane damper showed good efficiency in extremely low frequencies and seems promising for vibration suppression.

Keywords: low-frequency vibration; membrane damper; local resonance; bandgap

Citation: I, B.; Lee, J. Numerical and Experimental Study of Low-Frequency Membrane Damper for Tube Vibration Suppression. *Actuators* **2024**, *13*, 106. <https://doi.org/10.3390/act13030106>

Academic Editor: Ramin Sedaghati

Received: 4 January 2024

Revised: 2 March 2024

Accepted: 6 March 2024

Published: 8 March 2024



Copyright: © 2024 by the authors. Licensee MDPI, Basel, Switzerland. This article is an open access article distributed under the terms and conditions of the Creative Commons Attribution (CC BY) license (<https://creativecommons.org/licenses/by/4.0/>).

1. Introduction

Unwanted vibrations can cause significant problems for various systems and structures, and engineering principles must be employed to address them. Various sources, including machines, transportation, seismic activity, and human activity, can cause vibrations. The effects can be severe, ranging from damage to structures to malfunctioning sensitive equipment and processes. The goal of vibration isolation is to minimize or eliminate the transmission of vibrations from one system or component to another, thereby preserving the affected elements' integrity, performance, and functionality. Many types of engineering applications require vibration isolation. In industrial settings, heavy machinery can generate vibrations that may compromise nearby structures or affect the precision of delicate manufacturing processes. Vehicles and aircraft also create vibrations that can cause problems for passengers or sensitive equipment. In electronics, the performance of delicate instruments and devices can be significantly impacted by vibrations, leading to reduced accuracy or malfunction. To address these challenges, engineers use various techniques and technologies for vibration isolation. These may include isolators, dampers, and resilient materials designed to absorb, dissipate, or redirect vibrational energy. The field of vibration isolation encompasses both active [1–6] and passive methods [7–12], each with advantages and limitations. Active vibration control requires a power source, a feedback sensor, and a controller to generate and regulate the control force or moment. This technique has a broader operation bandwidth and can achieve multiple objectives simultaneously. Nevertheless, active vibration control has some drawbacks, namely, high cost, complexity, energy consumption, and stability and robustness issues. On the contrary, passive vibration control involves adding or modifying elements in the system, such as

springs, dampers, masses, or isolators, to change its natural frequency, damping ratio, or mode shape. Passive vibration control does not require any external power source, feedback sensor, or controller. It is relatively cheap, easy to implement, and robust to uncertainties and disturbances. However, passive vibration control has some limitations, such as low effectiveness at high frequencies, narrow bandwidth of operation, and trade-off between stiffness and damping.

In the last ten years, the capacity of phononic crystals to manipulate elastic waves has captured the interest of many researchers. The ability to forbid propagation in some frequency range for elastic waves (i.e., bandgap) has numerous applications in different fields, including vibration suppression. For example, Meng [13] indicated that the transmission of waves in particular frequency ranges and phononic band gaps can be obstructed through phononic crystals and metamaterials. The extension of band gaps in these materials is attributed to block mass variations. The design proposed, which is nearly periodic, is based on cuboid blocks connected by curved beams. The blocks have internal voids that adjust the local masses and generate a 3D rainbow phononic crystal. The results reveal that the proposed approach can create lightweight phononic crystal with a simple and manufacturable design. The attenuation bandwidths of these phononic crystals surpass those of equivalent periodic designs with equal mass, exhibiting more than twice the effectiveness. Shao [14] conducted a simulation and experimental investigation on the vibration reduction of low-frequency honeycomb phononic crystals. The results suggest that the honeycomb phononic crystal is a noteworthy solution for reducing vibration, particularly at lower frequencies. The authors designed a honeycomb phononic crystal using a chemigum plate and a steel column, calculated the bandgaps, and analyzed the vibration modes. The results showed that the honeycomb phononic crystal reduced vibration by up to 60 dB in the frequency range of 600–900 Hz, while a rubber plate only reduced it by about 20 dB. Yang et al. [15] described low-frequency elastic waves and vibration control mechanism of innovative phononic crystal thin plates. The plate is shown to have good band gap tuning and vibration attenuation effects. An innovative phononic crystal thin plate is proposed for controlling low-frequency vibration in practical engineering. Peng et al. [16] stated that in this article, the method of modeling, operating principle, and recommended specifications for acoustic metamaterial plates with multiple stopbands are presented. The metamaterial plate is designed to reduce vibrations by incorporating a two-degree of freedom mass-spring system within an isotropic plate. The metamaterial plate employs the principles of traditional vibration absorbers, as indicated by the results obtained. The stopbands' bandwidth can be increased by adjusting the absorber mass and the average mass of the isotropic plate. The paper also discusses the importance of damping ratios for quick response and wide stopbands. A sensitivity analysis on absorber resonant frequencies reveals significant sensitivity in the stopband regions. Wei [17] reported the vibration attenuation of 2D rainbow metamaterial plates with spatially varying stepped resonators. It is found that rainbow resonators can lead to broader vibration attenuation bands compared to periodic resonators. The additional mode shapes of the rainbow resonators break the complete bandgap of the periodic metamaterial plate into isolated narrower bandgaps, resulting in reduced vibration of the host plates. Broadening the attenuation band by nonperiodicity could help design plate structures with better vibration attenuation. The study also discusses the existence of bandgaps in elasto-acoustic metamaterials and the potential for vibration attenuation at low frequencies. The paper proposes metamaterial plates with rainbow-stepped resonators for obtaining broader vibration attenuation bands. The dynamic properties of periodic and rainbow metamaterial plates are compared, and it is concluded that the nonperiodic resonators' varied resonance frequencies contribute to the attenuation band's broadening. The study suggests that the investigated metamaterial plate can be extended to broader applications and provides data availability information.

With the latest scientific developments, membrane-type acoustic metamaterials have recently garnered significant attention. Yang [18] unveiled a novel concept of negative dynamic mass that indicates a phase difference between force and acceleration. These

materials demonstrate macroscopic behaviors beyond classical acoustics by negating the Newtonian assumptions. The fundamental building block of these materials is a circular elastic membrane with a fixed boundary. The authors have successfully utilized stacked membrane-type panels with varying operating frequencies to achieve optimal effectiveness across various frequencies. Given the weak elastic moduli of the membrane, small and finite samples can produce distinct low-frequency oscillation patterns. These findings hold substantial implications for the design and development of future acoustic metamaterials. Afterwards, scientists suggested other techniques for designing acoustic metamaterials to enhance their ability to insulate low-frequency sounds. They achieved strong and broad sound insulation in the low-frequency range [19–26].

In addition to excellent sound insulation, membrane resonators show potential applications as vibration isolators. Like in the sound isolation case, low elastic moduli shift resonance frequency to lower frequencies. Sun et al. [27] reported the experimental realization of the decorated membrane resonator, which offers a lightweight, compact, and effective low-frequency damper. Two dampers can significantly reduce the vibration amplitude at around 150 Hz with a weight of 0.6% of the host structure. According to a research study by Gao et al. [28], important design principles have been identified for the bilayer membrane-type metamaterial. By increasing the mass values of resonators and applying tensile stresses to membranes in each unit cell, the bandgap width can be expanded. Conversely, changing the periodicity of the unit cell has the opposite effect. In another study, Dong and colleagues [29] suggested a new metamaterial plate with double-mass membrane-type resonators (DMMRs). The results indicate that the suggested metamaterial plate possesses multiple band gaps caused by the cancellation of the shear forces in the plate by the reaction forces produced by the first two resonances of the resonators. The research suggests that the presence and size of the two band gaps are strongly linked to the mass ratio between the resonator and the host plate. In another study, Sun [30] described an experimental investigation of a vibration damper composed of acoustic metamaterials. This paper presents the experimental results of a vibration damper comprising acoustic metamaterials attached to a rectangular steel plate. The damper reduces vibrating plate resonance magnitudes by up to 42 dB and provides an overall vibration reduction of 24.7 dB in the 100–1200 Hz frequency range. The damper shows potential for use in aerospace vehicles. Comparison experiments with a commercial rubber plate show that the acoustic metamaterial structure performs better in lower and higher frequency ranges. Shen et al. [31] discuss phononic crystals and a periodic pipe structure to control vibrations in piping systems. The calculations are based on the Timoshenko beam model and the Bragg scattering mechanism of phononic crystals. The results show that the vibration band gaps effectively attenuate vibrations. The research provides a reference for the design and vibration control of liquid-filled composite pipelines. The paper also calculates the band structure of flexural, longitudinal, and torsional vibrations using the transfer matrix method. The results demonstrate the existence of vibration band gaps in a 3D periodic pipe structure. The paper emphasizes the importance of considering shear distortion and section moment of inertia in accurately calculating flexural vibration frequency response functions. The density, Young's modulus, and shear modulus of epoxy and steel are provided to calculate the band structures of a straight periodic pipe. Understanding the vibration properties of this system is crucial. Manushyna et al. [32] studied the application of vibroacoustic metamaterials for structural vibration reduction in space structures. The technology of vibroacoustic metamaterials is applied to representative scaled-down launchers and satellite components. It was shown to lower vibrations across a broad spectrum of frequencies, which is beneficial for handling. Moreover, vibroacoustic metamaterials make using composite materials for rocket components possible. According to Janssen et al. [33], vibroacoustic metamaterials that are locally resonant are effective in reducing noise and vibration; however, these materials often experience a significant drop in performance after achieving peak insulation, which limits their usefulness. To break the limitation, a multiresonant metamaterial panel was developed and compared

to a conventional panel, demonstrating improved performance after the peak insulation. Ma et al. [34] suggested a technique to dampen low-frequency vibrations using ultralight locally resonant plate-type units as dampers, which have a designable band gap property to absorb and localize structural vibration in a predefined band gap range. These dampers can be as light as 0.3% of the objective vibration structure, making them highly suitable for industry applications. Wang [35] proposed a broadband damping method using multiple damping units to achieve vibration absorption across a wide frequency range. By integrating units with different frequency ranges, a linear superposition of the absorption bandwidth can be achieved, overcoming the limitations of traditional dynamic vibration absorbers or metamaterial dampers with narrow working bands. This design optimizes each subunit's working bandwidth, significantly increasing the available design parameters. The damper device and subunits are small, resulting in lower additional mass compared to traditional dynamic vibration absorbers. The proposed method and device have potential applications in suppressing low-frequency vibrations in various machinery and equipment. Li and colleagues [36] noted that a metamaterial plate with multi bandgaps is proposed for vibration suppression by integrating membrane-mass structures into a honeycomb sandwich structure. The proposed metamaterial exhibits excellent vibration suppression performance and designability. Yu and colleagues [37] reported an integrated load-bearing vibration-isolation supporter with decorated metamaterial absorbers. Without altering the metallic support structure, a steel support column offers the necessary load-bearing rigidity. Additionally, some lightweight subwavelength local resonance units are integrated to prevent the propagation of elastic waves and absorb the vibration of the support structure. The vibration-absorbing unit's band gap can be customized based on parameters such as the mass block radius, plate thickness, frame height, and beam width.

The aim of the current study is an experimental investigation of low-frequency vibration attenuation. The tubes with small diameters (outer diameter to 16 mm) used in different systems, for example, condition systems, are vulnerable to continuous low-frequency vibration, leading to fatigue. Due to this and the fact that it is not covered in the existing works, the authors propose the membrane resonator to suppress the vibration in tubes in the frequency range from 100 Hz to 150 Hz.

2. Dispersion Curves and Bandgap Configuration

The resonance of the mechanical system is described by a well-known Equation (1) that is suitable for the prediction of the first bandgap [38]:

$$f_r = \frac{1}{2\pi} \sqrt{\frac{k}{m}} \quad (1)$$

where k —stiffness, m —mass. To achieve low-frequency resonance, there are two possible approaches: decreasing the stiffness or increasing the mass. However, increasing the mass is unsuitable for the current case since the tubes are in focus, which are usually lightweight. The different types of silicone can provide the low stiffness required. Additionally, since the tube has axial symmetry, for the sake of simplicity, the resonator also has axial symmetry.

The first step of the study of the proposed resonator is in the dispersion curves calculation, which can show the frequency range where the propagation of the waves (longitudinal, torsional and flexural guided waves) is restricted; in other words, the waves have a bandgap. For that, the governing Equation (2) in eigenfrequency formulation (3) is used.

$$\rho \frac{\partial^2 u}{\partial t^2} = \nabla \sigma \quad (2)$$

$$\rho \lambda^2 u = \nabla \sigma \quad (3)$$

where ρ —density, u —displacement, ∇ —nabla operator, σ —stress tensor, $\lambda = -j\omega$ —eigenfrequency.

Threatening the resonator as an infinite chain of phononic crystals allows the application of the Floquet boundary condition and the calculation of wave behavior in the first irreducible Brillouin zone [39]. Because of axial symmetry, geometry can be reduced from 3D to 2D axisymmetric, with a circumferential wavenumber equal to an integer number. By solving the eigenvalue problem, the dispersion curve can be obtained.

The described procedure was performed using commercial software COMSOL ver. 6.1 based on the finite element method. A copper tube was chosen as a host structure because of the wide range of usage. The silicone membrane resonator with an additional mass and a frame are attached to the tube. The material properties of copper and silicone are provided in Table 1.

Table 1. Material properties.

	Young's Modulus, GPa	Density, kg/m ³	Poisson Ratio
Silicone	Shore A 70 (5.5 MPa)	1100	0.44
Copper	110	8960	0.35

The hardness s of the silicone can be converted to Young's modulus approximately by the Gent Equation (4) [40] (result in MPa):

$$E = \frac{0.0981(56 + 7.66s)}{0.137505(254 - 2.54s)} \approx 5.5(s = 70) \quad (4)$$

The overall length of the unit cell is 50 mm, with 1 mm wall thickness of the tube, 5 × 15 mm frame, 10 × 20 mm mass, and 1 × 9 mm membrane (Figure 1). Considering that the Floquet boundary condition is applied to the tube's ends, solving the eigenfrequency problem in the wavenumber domain in the range $[0, \frac{\pi}{L}]$, where L —unit cell length, gives the set of frequencies for the given wavenumber and circumferential wavenumber $m = 0, 1, 2$.

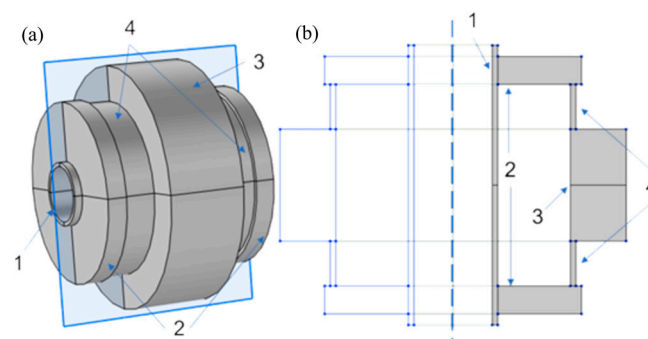


Figure 1. (a) 3D and (b) 2D axisymmetric representation of the proposed membrane resonator. 1—tube, 2—frame, 3—additional mass, 4—membrane, dashed line—axis of symmetry.

The mesh size can be defined by many criteria, for example, by defining the necessary among the points at the wavelength [41]. For the model, the number of points is equal to 10, so the mesh size is 1 mm. The corresponding model is discretized by 418 quadratic elements in 4942 degrees of freedom. Computation on a Dell workstation took 7 min 15 s, which is relatively fast, but the increased complexity of the model (e.g., material anisotropy) increases the computational time. Potentially, the modification of the model, e.g., modified Drucker–Prager model [42], can be implemented to enhance the accuracy and decrease the computation time.

In Figure 2a, the $k-f$ dispersion curve is depicted. Firstly, multiple bandgaps can be observed, for example, between longitudinal guided wave modes $L(0,1)$ and $L(0,2)$, flexural waves $F(1,1)$ and $F(1,2)$, $F(1,2)$ and $F(1,3)$, or torsional wave $T(0,1)$ and $T(0,2)$ (exist higher than 300 Hz and not presented in graph), which makes the proposed resonator suitable for any vibration type. Also, it is interesting to note the curve behavior itself; all curves turn

into a straight line, which means the mode shape transforms from the motion of the entire unit cell into the motion of the membrane resonator (Figure 2b,c).

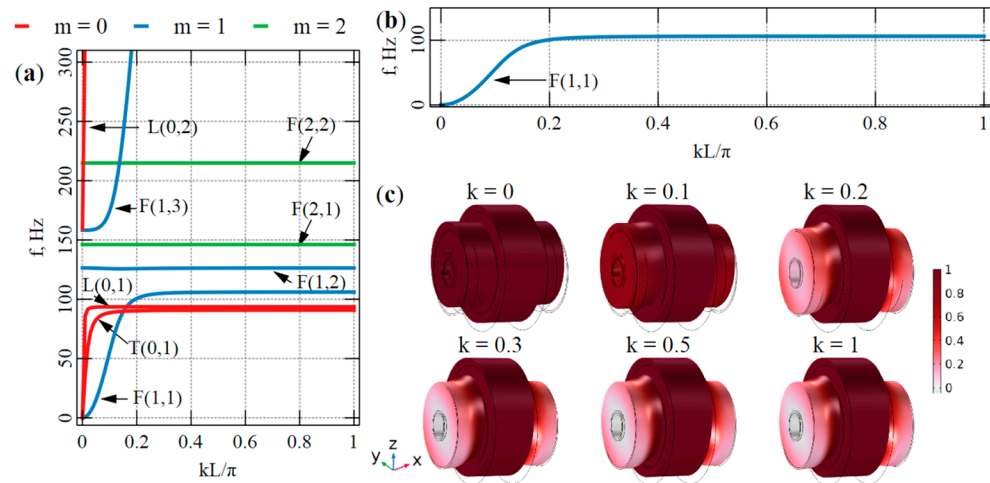


Figure 2. (a) Dispersion curves. Different colors represent different values of the circumferential wavenumber m . (b) Dispersion curve of $F(1,1)$ and (c) mode shape in different values of wavenumber k associated with $F(1,1)$.

Since the flexural wave is dominant among all waves and the higher flexural waves ($m > 1$) represent the resonator's motion, only the flexural wave with $m = 1$ is interesting. For this wave, bandgaps between $F(1,1)$ – $F(1,2)$ and $F(1,2)$ – $F(1,3)$ can be observed. As $F(1,2)$ is a straight line, it can be excluded. Overall, the bandgap is 106 Hz to 158 Hz, where the first flexural wave does not exist.

The complete characterization of the dynamic impact of a deep-subwavelength object with linear internal vibrational degrees of freedom on a vibrational host body can be achieved by determining its effective mass. The effective mass is calculated based on the hybridization method [43] to explain the resonator's behavior. To define the effective mass m_{eff} , Newton's second law is employed Equations (5)–(7), expressed as follows:

$$m_{ij}^{eff} = \rho_{ij}^{eff} V = \frac{\langle F_i \rangle}{\langle a_j \rangle} \quad (5)$$

$$\langle F_i \rangle = \frac{1}{S} \int_S \sigma_{ik} n_k ds \quad (6)$$

$$\langle a_j \rangle = \frac{1}{V} \int_V a_j ds \quad (7)$$

where ρ_{eff} —effective mass density, V —unit cell volume, F —force, a —acceleration, $\langle \bullet \rangle$ —volume average, S —boundary area, σ —local stress, and n —boundary unit normal vector. Since the flexural wave is interested, only the Z component of the force and acceleration is considered.

Figure 3 depicts a calculated relative effective mass (the total static mass of the unit cell is 77 g). It is seen that the closer the system is to the bandgap, the higher the effective mass of the unit cell, indicating a good vibration suppression effect to be expected. A straight line inside the bandgap is related to $F(1,2)$ in Figure 2a.

Before manufacturing the proposed resonator, it is interesting to analyze the bandgap frequencies' sensitivity on the deviation of membrane geometry. For that, a parametric study was performed, with the membrane thickness varying from 0.5 mm to 2 mm and the membrane length varying from 1.5 mm to 19 mm. A closer look at Figure 2a shows

that four frequencies can be noted. It is the maximum frequency of the F(1,1), minimum and maximum frequency of the F(1,2) and minimum frequency of F(1,3). These frequencies form the bandgap and are depicted in Figure 4. Firstly, the membrane thickness shifts the bandgap at higher frequencies and does not change the shape of the F(1,2). Secondly, the membrane length shows the opposite behavior; with the increased membrane length, the bandgap tends to lower-frequency forms between F(1,1) and F(1,2).

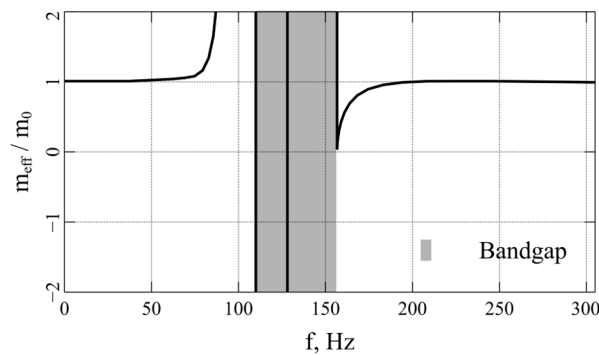


Figure 3. Relative effective mass of the unit cell.

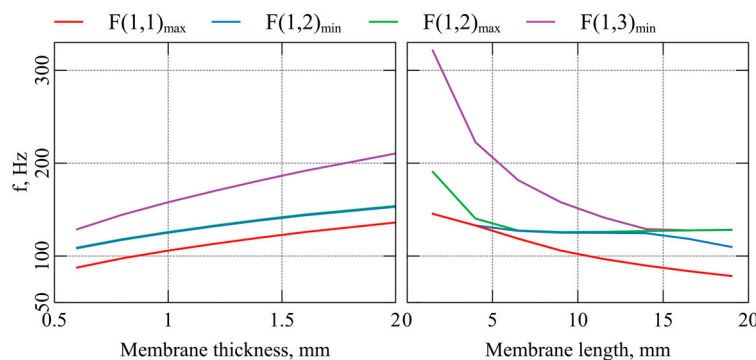


Figure 4. Bandgap frequencies versus membrane thickness and length.

3. Experimental Setup

The proposed resonator (Figure 5) was made by silicone (presented in Table 1) and printed by a Sandraw (Taichung, Taiwan) silicone 3D printer with dimensions the same as in the previous section, except the internal diameter is slightly lower 16 mm (~15.6 mm). According to the manufacturer, the silicone 3D printed has a 0.4 mm resolution, so the bandgap should be at the predicted frequencies. The mass of the resonator is 56 g.



Figure 5. Printed membrane resonator.

The copper tube with a 16 mm outer diameter, 1 mm wall thickness, and 1430 mm length was used as a host structure and clamped on an aluminum frame with silicone inserts on both ends. The tube lay on the aluminum frame with soft silicone inserts to minimize unnecessary external vibration. The resonator was attached to the tube without

glue in three locations to avoid mode shape nodes. The roving hammer technique was used to accurately depict wave propagation in the tube with the resonator. Figure 6 shows the scheme of the experimental setup. A PCB 084A17 impact hammer was used to excite the vibration of the tube with the resonator in nine different points with 100 mm spacing between points. The impact hammer connected to the Optomet (Darmstadt, Germany) laser doppler vibrometer and sent the trigger signal to start the measurement. The PC with the Optoscan ver. 2.15.5 software controls the entire process (start–stop measurement) and post-processes the measured data.

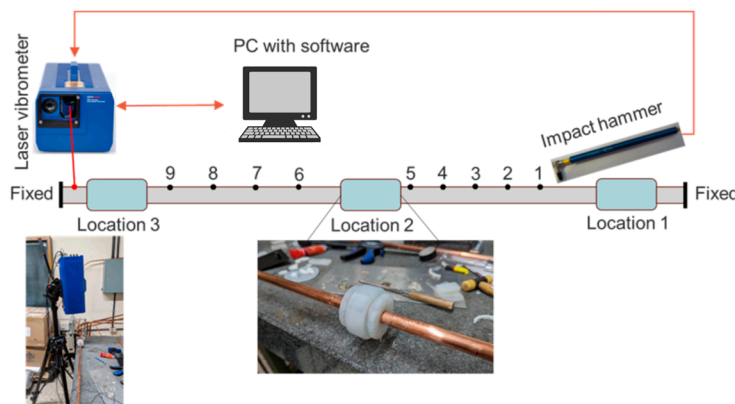


Figure 6. Experimental setup. Black points—excitation points; red points—measurement points.

After triggering, the laser vibrometer measures the velocity amplitude for 16 s for better frequency resolution (example of measured data depicted in Figure 7). After that, the raw measured signal is windowed by an exponential function.

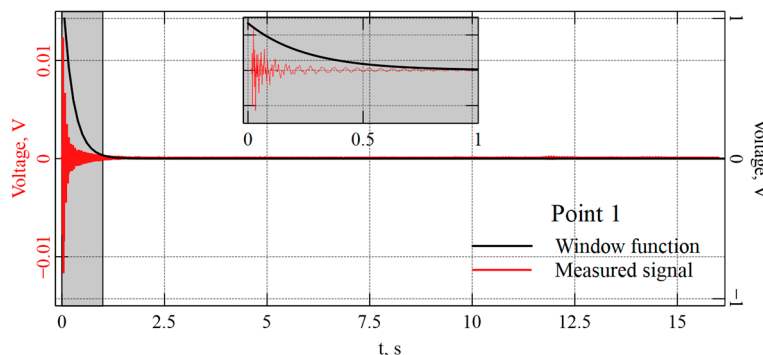


Figure 7. Example of measured signal with an exponential window function.

A linear mechanical system with excitation $x(t)$ and response $y(t)$ signals can be characterized by the frequency response function (FRF) as in Equations (8)–(11):

$$FRF = \frac{Y(f)}{X(f)} = \frac{\langle G_{YX}(f) \rangle}{\langle G_{XX}(f) \rangle} = \frac{\langle G_{YY}(f) \rangle}{\langle G_{XY}(f) \rangle} \quad (8)$$

$$\langle G_{YX}(f) \rangle = \frac{\sum_k X_k(f) \cdot Y_k^*(f)}{N_{av}} \quad (9)$$

$$\langle G_{XX}(f) \rangle = \frac{\sum_k X_k(f) \cdot X_k^*(f)}{N_{av}} \quad (10)$$

$$x(t) \xrightarrow{FFT} X(f), y(t) \xrightarrow{FFT} Y(f) \quad (11)$$

where $X(f)$, $Y(f)$ —fast Fourier transform of the $x(t)$ and $y(t)$ respectively, $\langle G_{XX}(f) \rangle$, $\langle G_{YX}(f) \rangle$ —average auto power spectrum and cross power spectrum, respectively, N_{av} —number of repetitions.

tions of excitation. The average values are used to make a spectrum less noisy, so each point was excited $N_{av} = 4$ times.

4. Results

Figure 8 compares the FRF of the bare tube and tube with the membrane resonator in three locations (see Figure 6) and in nine different points of excitation. The bare tube in the frequency range 0–200 Hz has three peaks marked 1, 2, and 3 in Figure 8. The first peak is related to the silicone inserts; the tube is “bouncing” on the silicone. The second peak is the first flexural resonance of the tube, and the third peak is the second flexural resonance of the tube. Due to the initial objective to suppress the vibration in the 100–150 Hz frequency range, the third peak is the target.

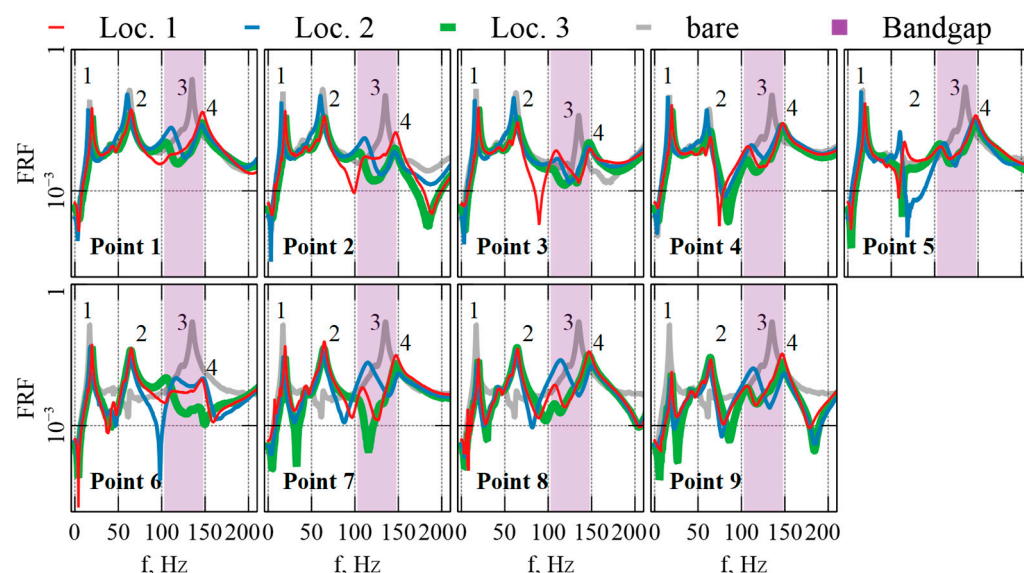


Figure 8. The FRF for different points of excitation. 1, 2, 3, 4—amplitude peaks. Loc. 1—location 1, Loc. 2—location 2, Loc. 3—location 3 in Figure 6.

As established in Section 2, the array of proposed resonators should create the bandgap for the flexural wave in the frequency range from 106 Hz to 158 Hz (yellow region) and eliminate the third resonance peak, which can be observed in Figure 8. The results due to the excitation at different points are clearly in line with each other. As can be seen, the attenuation representing the bandgap zone can be detected in all measured responses.

In addition, four small peaks at the boundaries of the bandgap can be observed. According to Section 2, these peaks are related to the resonance of the membrane resonator. In the eigenfrequency study, an infinite number of resonators was assumed, but the experiment shows that a single resonator has a bandgap, too.

5. Discussion

Depicted results indicate the bare tube’s amplitude reduction at bandgap and other resonance frequencies. The tube motion and resonator movement are in phase below the stopband zone, resulting in a higher overall structure mass. This is partly due to the relatively high loss factor of the resonators compared to the copper tube. Experimental results show the existence of the resonator’s modes, which are marked as 4 in Figure 8; potentially, this peak can be made higher by adding additional resonators, eliminating the advantages of the proposed resonator. The single-element resonator shows good performance and agreement with previous studies in field of membrane dampers, showing the amplitude drop in frequencies related to the bandgap and extremum of the effective mass at frequency closer to the bandgap. The resonator solution’s effectiveness in the stopband zone is further enhanced by the broadband decrease in the tube’s acceleration

level, which enhances the tube's overall performance. In comparison with the existing works (for example [31,35,38]), which offer array of the cells, the proposed resonator offers single-element, lightweight damper for tubes, which effectively works in the 100–150 Hz range. Unfortunately, the resonance peaks around 20 Hz and 60 Hz are out of scope. Still, they are more likely for suppression, especially 20 Hz, since there are no lightweight and compact solutions for such extremely low frequencies. However, studying how to achieve the bandgap at extremely low frequencies with relatively large bandgap, meaning the study of the dimensions, shape, and materials, can potentially offer a solution. Moreover, suppose the additional studies perform similarly to a proposed single-element resonator. In that case, several resonators (each for a specific resonance peak) can be stacked, and the interaction between them can be examined.

6. Conclusions

In conclusion, the proposed membrane resonator successfully eliminates the resonance peak in the target frequency range. Initially, the FEM and Floquet boundary condition showed the bandgap in 106–158 Hz. Afterwards, the proposed membrane resonator was printed by a Sandraw silicone 3D printer, and a single resonator was added to the tube. A rover hammer technique was used to characterize the behavior of the tube. Structural vibration was measured by a laser vibrometer. Averaging was used to reduce the noise in an FRF spectrum. The resulting FRF shows the predicted bandgap. A single resonator is enough, which makes the proposed resonator lightweight, compact, and independent of the location solution for vibration suppression. Because of the silicone that was used for printing, there was no need to glue the resonator to the tube. By adjusting the stiffness and mass of the resonator, it is possible to tune up the “location” of the bandgap; for example, by lowering the stiffness of the resonator, it is possible to achieve the bandgap at 50 Hz or lower to eliminate, for example, peak 2 in Figure 8.

Author Contributions: Conceptualization, B.I. and J.L.; methodology, B.I. and J.L.; validation, B.I.; formal analysis, B.I.; resources, J.L.; data curation, B.I.; writing—original draft preparation, B.I. and J.L.; writing—review and editing, J.L.; visualization, B.I.; funding acquisition, J.L. All authors have read and agreed to the published version of the manuscript.

Funding: This work was supported by Korea Institute of Energy Technology Evaluation and Planning (KETEP) grant funded by the Korea government (MOTIE) (No. 20217410100100 and No. 20214000000480, Development of R&D engineers for combined cycle power plant technologies).

Data Availability Statement: Data are contained within the article.

Conflicts of Interest: The authors declare no conflicts of interest.

References

1. Fuller, C.C.; Elliott, S.; Nelson, P.A. *Active Control of Vibration*; Academic Press: Cambridge, MA, USA, 1996.
2. Preumont, A. *Vibration Control of Active Structures: An Introduction*; Springer: Berlin/Heidelberg, Germany, 2018; Volume 246.
3. Karnopp, D.; Crosby, M.J.; Harwood, R.A. Vibration control using semi-active force generators. *J. Eng. Ind.* **1974**, *96*, 619–626. [[CrossRef](#)]
4. Maurini, C.; Dell’Isola, F.; Del Vescovo, D. Comparison of piezoelectronic networks acting as distributed vibration absorbers. *Mech. Syst. Signal Process.* **2004**, *18*, 1243–1271. [[CrossRef](#)]
5. Ferrari, G.; Amabili, M. Active vibration control of a sandwich plate by non-collocated positive position feedback. *J. Sound Vib.* **2015**, *342*, 44–56. [[CrossRef](#)]
6. Omidi, E.; Mahmoodi, S.N.; Shepard, W.S., Jr. Multi positive feedback control method for active vibration suppression in flexible structures. *Mechatronics* **2016**, *33*, 23–33. [[CrossRef](#)]
7. Kim, S.M.; Wang, S.; Brennan, M.J. Dynamic analysis and optimal design of a passive and an active piezo-electrical dynamic vibration absorber. *J. Sound Vib.* **2011**, *330*, 603–614. [[CrossRef](#)]
8. Harne, R.L. On the linear elastic, isotropic modeling of poroelastic distributed vibration absorbers at low frequencies. *J. Sound Vib.* **2013**, *332*, 3646–3654. [[CrossRef](#)]
9. Rao, S.S. *Vibration of Continuous Systems*; John Wiley & Sons: Hoboken, NJ, USA, 2019.
10. Boas, M.L. *Mathematical Methods in the Physical Sciences*; John Wiley & Sons: Hoboken, NJ, USA, 2006.
11. Ishida, Y. Recent development of the passive vibration control method. *Mech. Syst. Signal Process.* **2012**, *29*, 2–18. [[CrossRef](#)]

12. Balaji, P.S.; Karthik SelvaKumar, K. Applications of nonlinearity in passive vibration control: A review. *J. Vib. Eng. Technol.* **2021**, *9*, 183–213. [[CrossRef](#)]
13. Meng, H.; Bailey, N.; Chen, Y.; Wang, L.; Ciampa, F.; Fabro, A.; Elmadih, W. 3D rainbow phononic crystals for extended vibration attenuation bands. *Sci. Rep.* **2020**, *10*, 18989. [[CrossRef](#)]
14. Shao, H.B.; Chen, G.P.; He, H.; Jiang, J.H. Simulation and experimental investigation of low-frequency vibration reduction of honeycomb phononic crystals. *Chin. Phys. B* **2018**, *27*, 126301. [[CrossRef](#)]
15. Yang, H.Y.; Cheng, S.L.; Li, X.F.; Yan, Q.; Wang, B.; Xin, Y.J.; Zhao, Q.X. Low frequency elastic waves and vibration control mechanism of innovative phononic crystal thin plates. *Phys. B Condens. Matter* **2023**, *667*, 415189. [[CrossRef](#)]
16. Peng, H.; Pai, P.F.; Deng, H. Acoustic multi-stopband metamaterial plates design for broadband elastic wave absorption and vibration suppression. *Int. J. Mech. Sci.* **2015**, *103*, 104–114. [[CrossRef](#)]
17. Wei, W.; Chronopoulos, D.; Meng, H. Broadband vibration attenuation achieved by 2D elasto-acoustic metamaterial plates with rainbow stepped resonators. *Materials* **2021**, *14*, 4759. [[CrossRef](#)]
18. Yang, Z.; Mei, J.; Yang, M.; Chan, N.H.; Sheng, P. Membrane-Type Acoustic Metamaterial with Negative Dynamic Mass. *Phys. Rev. Lett.* **2008**, *101*, 204301. [[CrossRef](#)]
19. Naify, C.J.; Chang, C.M.; McKnight, G.; Nutt, S. Transmission loss of membrane-type acoustic metamaterials with coaxial ring masses. *J. Appl. Phys.* **2011**, *110*, 124903. [[CrossRef](#)]
20. Naify, C.J.; Chang, C.M.; McKnight, G.; Scheulen, F.; Nutt, S. Membrane-type metamaterials: Transmission loss of multi-celled arrays. *J. Appl. Phys.* **2011**, *109*, 104902. [[CrossRef](#)]
21. Li, J.; Fan, X.; Li, F. Numerical and experimental study of a sandwich-like metamaterial plate for vibration suppression. *Compos. Struct.* **2020**, *238*, 111969. [[CrossRef](#)]
22. Huang, T.Y.; Shen, C.; Jing, Y. Membrane-and plate-type acoustic metamaterials. *J. Acoust. Soc. Am.* **2016**, *139*, 3240–3250. [[CrossRef](#)] [[PubMed](#)]
23. Ma, F.; Huang, M.; Wu, J.H. Acoustic metamaterials with synergetic coupling. *J. Appl. Phys.* **2017**, *122*, 215102. [[CrossRef](#)]
24. Ma, F.; Xu, Y.; Wu, J.H. Shell-type acoustic metasurface and arc-shape carpet cloak. *Sci. Rep.* **2019**, *9*, 8076. [[CrossRef](#)] [[PubMed](#)]
25. Gao, N.; Wu, J.; Lu, K.; Zhong, H. Hybrid composite meta-porous structure for improving and broadening sound absorption. *Mech. Syst. Signal Process.* **2021**, *154*, 107504. [[CrossRef](#)]
26. Jiménez, N.; Romero-García, V.; Pagneux, V.; Groby, J.P. Rainbow-trapping absorbers: Broadband, perfect and asymmetric sound absorption by subwavelength panels for transmission problems. *Sci. Rep.* **2017**, *7*, 13595. [[CrossRef](#)]
27. Sun, L.; Au-Yeung, K.Y.; Yang, M.; Tang, S.T.; Yang, Z.; Sheng, P. Membrane-type resonator as an effective miniaturized tuned vibration mass damper. *AIP Adv.* **2016**, *6*, 085212. [[CrossRef](#)]
28. Gao, C.; Halim, D.; Yi, X. Study of bandgap property of a bilayer membrane-type metamaterial applied on a thin plate. *Int. J. Mech. Sci.* **2020**, *184*, 105708. [[CrossRef](#)]
29. Thelen, M.D.; Dauber, J.A.; Stoneman, P.D. Characteristics of band gaps of a metamaterial plate with membrane-type resonators based on the energy approach. *Thin-Walled Struct.* **2023**, *191*, 110930. [[CrossRef](#)]
30. Sun, L. Experimental investigation of vibration damper composed of acoustic metamaterials. *Appl. Acoust.* **2017**, *119*, 101–107. [[CrossRef](#)]
31. Shen, H.; Wen, J.; Yu, D.; Wen, X. The vibrational properties of a periodic composite pipe in 3D space. *J. Sound Vib.* **2009**, *328*, 57–70. [[CrossRef](#)]
32. Manushyna, D.; Hülsebrock, M.; Kuisl, A.; Vivo, A.D.; Heloret, P.; Atzrodt, H.; Rapp, S. Application of vibroacoustic metamaterials for structural vibration reduction in space structures. *Mech. Res. Commun.* **2023**, *129*, 104090. [[CrossRef](#)]
33. Janssen, S.; Van Belle, L.; de Melo Filho NG, R.; Desmet, W.; Claeys, C.; Deckers, E. Improving the noise insulation performance of vibro-acoustic metamaterial panels through multi-resonant design. *Appl. Acoust.* **2023**, *213*, 109622. [[CrossRef](#)]
34. Ma, F.; Cai, Y.; Wu, J.H. Ultralight plat-type vibration damper with designable working bandwidth and strong multi-peak suppression performance. *J. Phys. D Appl. Phys.* **2020**, *54*, 055303. [[CrossRef](#)]
35. Wang, X.; Pang, Y.; Hui Wu, J.; Ma, F. A broadband metamaterial damper design based on synergetic coupling among multi-cells. *Appl. Acoust.* **2023**, *206*, 109303. [[CrossRef](#)]
36. Li, J.; Zhang, Y.; Fan, X.; Li, F. Multi bandgaps design of sandwich metamaterial plate with embedded membrane-type resonators. *J. Sandw. Struct. Mater.* **2023**, *25*, 311–329. [[CrossRef](#)]
37. Yu, R.; Rui, S.; Wang, X.; Ma, F. An integrated load-bearing and vibration-isolation supporter with decorated metamaterial absorbers. *Int. J. Mech. Sci.* **2023**, *253*, 108406. [[CrossRef](#)]
38. Liu, Z.; Zhang, X.; Mao, Y.; Zhu, Y.Y.; Yang, Z.; Chan, C.T.; Sheng, P. Locally resonant sonic materials. *Science* **2000**, *289*, 1734–1736. [[CrossRef](#)] [[PubMed](#)]
39. Nateghi, A.; Sangiuliano, L.; Claeys, C.; Deckers, E.; Pluymers, B.; Desmet, W. Design and experimental validation of a metamaterial solution for improved noise and vibration behavior of pipes. *J. Sound Vib.* **2019**, *455*, 96–117. [[CrossRef](#)]
40. Gent, A.N. On the relation between indentation hardness and Young's modulus. *Rubber Chem. Technol.* **1958**, *31*, 896–906. [[CrossRef](#)]
41. Domaneschi, M. Experimental and numerical study of standard impact tests on polypropylene pipes with brittle behaviour. *Proc. Inst. Mech. Eng. Part B J. Eng. Manuf.* **2012**, *226*, 2035–2046. [[CrossRef](#)]

42. Domaneschi, M.; Perego, U.; Borgqvist, E.; Borsari, R. An industry-oriented strategy for the finite element simulation of paperboard creasing and folding. *Packag. Technol. Sci.* **2017**, *30*, 269–294. [[CrossRef](#)]
43. Liu, X.N.; Hu, G.K.; Sun, C.T.; Huang, G.L. Wave propagation characterization and design of two-dimensional elastic chiral metacomposite. *J. Sound Vib.* **2011**, *330*, 2536–2553. [[CrossRef](#)]

Disclaimer/Publisher’s Note: The statements, opinions and data contained in all publications are solely those of the individual author(s) and contributor(s) and not of MDPI and/or the editor(s). MDPI and/or the editor(s) disclaim responsibility for any injury to people or property resulting from any ideas, methods, instructions or products referred to in the content.